Szalai, R., & Osinga, HM. (2007). *Invariant polygons in systems with grazing-sliding*. http://hdl.handle.net/1983/948

Early version, also known as pre-print

Link to publication record in Explore Bristol Research
PDF-document

Invariant polygons in systems with grazing-sliding

R. Szalai[*] and H.M. Osinga[†]

7th August 2007

Abstract

We investigate generic three-dimensional non-smooth systems with a periodic orbit near grazing-sliding. We assume that the periodic orbit is unstable with complex multipliers so that two dominant frequencies are present in the system. Because grazing-sliding induces a dimension loss and the instability drives every trajectory into sliding, the attractor of the system will consist of forward sliding orbits. We analyze this attractor in a suitably chosen Poincaré section using a three-parameter generalized map that can be viewed as a normal form. We show that in this normal form the attractor resides on a polygonal-shaped invariant set and classify the number of sides as a function of the parameters. Furthermore, for fixed values of parameters we investigate the one-dimensional dynamics on the attractor.

There are several physical [5, 7], biological [16] and engineering [3, 24] systems that are best described using piecewise-smooth models. In these systems the phase space is partitioned by smooth codimension-one hypersurfaces so that different vector fields govern the dynamics depending on which side of the surface the actual system state is. At the partitioning boundary the vector field is typically not continuous. Due to this discontinuity, trajectories either cross the surfaces or leave them invariant, which is called *sliding* [9]. In mechanical systems with friction this is equivalent to a sticking motion. Sliding parts of the switching surface are strongly attracting so that nearby orbits reach the surface in finite time unlike in smooth systems, where invariant manifolds are reached in infinite time. As a result, in a system with sliding the dynamics is noninvertible in some parts of the phase space. We consider the case where all orbits are eventually trapped in a neighbourhood of the switching surface such that they will contain sliding segments. This means that an attractor exists and it is obtained from the forward trajectories of points where the switching surface ceases to be invariant. In a two-dimensional Poincaré map of a three dimensional piecewise-smooth system this

---

[*]Bristol Centre for Applied Nonlinear Matematics, University of Bristol, University Walk, Bristol, BS8 1TR (r.szalai@bristol.ac.uk)

[†]Bristol Centre for Applied Nonlinear Matematics, University of Bristol, University Walk, Bristol, BS8 1TR (h.m.osinga@bristol.ac.uk)

attractor consist of the forward images of a line. We investigate the case when this attractor is polygonal-shaped and occurs as a result of a bifurcation where a periodic orbit becomes unstable due to the removal of its sliding segment. This phenomenon is similar to a supercritical Neimark-Sacker bifurcation in the sense that the polygonal-shaped attractor resembles a torus. On the other hand, the attractor is not a topological circle and its intrinsic dynamics can be more complicated than is possible on a smooth torus.

1   Introduction

We are concerned with a focus-type unstable periodic orbit that is close to grazing with a switching surface containing a sliding region. We show that a polygonal-shaped attractor coexists with the unstable periodic orbit, provided it is close enough to grazing. If we were to change a parameter such that the orbit starts to slide, then the periodic orbit becomes stable and the polygonal-shaped attractor is gone. Hence, we could think of this phenomenon as a supercritical Neimark-Sacker bifurcation. The bifurcation occurs when the sliding region vanishes from the periodic orbit through grazing. At the grazing point the orbit is still stable, after grazing it becomes unstable and a polygonal-shaped attractor is born. Note that the bifurcation is mediated by the presence of a sliding region. If we disregard the switching, the stability properties of the periodic orbit typically do not change in the neighbourhood of the bifurcation (it remains unstable). As it turns out, the polygonal-shaped attractor is not a topological circle, because the dynamics extends to the lines drawn through the sides and is not restricted to the sides of the polygon. Our goal is to shed light on the question what is the appropriate equivalent of a smooth torus in a piecewise-smooth system.

Our motivating example is a forced friction oscillator on a belt, which was studied extensively in the literature [1, 8, 12, 14]. Due to discontinuities of the friction force the mathematical model is only piecewise-smooth. The switching surface is defined by the velocity at which the friction force changes sign. If the friction force on the switching surface can balance the external forces and the inertia of the mass then the block sticks to the surface; this is mathematically the sliding region. Otherwise the block mass leaves the stick phase and starts to slip. An alternating sequence of these phases is referred to as stick-slip motion, which can be periodic, quasi-periodic or even chaotic as we will see later. The dynamics of stick-slip motion can be analyzed by different techniques including *phase maps* [18], *event maps* [17] and *discontinuity maps* [6]. In this paper we take the latter approach. We construct a local piecewise-linear Poincaré map and devise a three-parameter normal form, that can be used to study the phenomenon in greater detail. We show that for certain parameter values the attractor resides on an invariant polygon, which has different number of sides depending on the parameters. For a particular set of parameter values we also show how chaotic motion develops in the system.

In [21] periodic orbits in delayed relay systems are studied, where the period is close
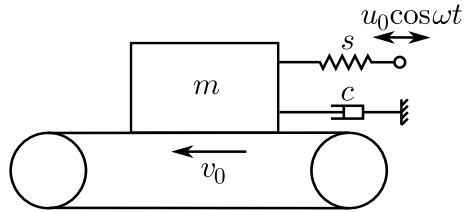
Figure 1: A forced linear oscillator on a belt with friction.

to the delay. In this case the local Poincaré map has different dimensions depending on how many times a trajectory crosses the switching surface during a delay interval. Therefore, the global Poincaré map includes projections that causes the same type of phenomena as sliding in piecewise-smooth ordinary differential equations and the appearance of invariant polygons. Invariant polygons can also arise in other types of piecewise-smooth systems, e.g., in the macroeconomics model of [22], or in a normal form dervied at a corner collision bifurcation [26] due to different mechanisms.

The paper is organized as follows. In the next section we describe our friction oscillator and obtain a Poincaré map with the help of the discontinuity map technique. In section 3, we introduce a three-parameter normal form map, and show that it has an invariant polygon-shaped attractor. We calculate the number of sides of the polygon ans investigate how it depends on the parameters. We also demonstrate the complicated dynamics that can occur on the attractor. In section 4 we summarize our results and discuss future directions of research.

2   The friction oscillator

We consider a one-degree-of-freedom oscillator (see Fig. 1) with block mass m, spring s and damper c. The block mass is sliding on a moving belt and is forced through the spring. We assume that there is friction between the mass and the belt, which induces a friction force with a decreasing slope near zero relative velocity. After rescaling time by the natural frequency of the oscillator, the equation of motion for the displacement x reads

$$\ddot{x} + 2\zeta\dot{x} + x = \operatorname{sgn}(v_0 - \dot{x})F_s - \kappa(v_0 - \dot{x}) + u_0 \cos \omega t, \qquad (1)$$

where ζ is the relative damping, F_s is the maximal steady friction force, κ is the slope of the friction force, v_0 is the speed of the belt, u_0 is the forcing amplitude and ω is the forcing (angular) frequency. The trivial periodic orbit of the system is a harmonic vibration, which can be obtained by substituting the ansatz $a + b\sin \omega t + c\cos \omega t$ into (1) and solving for a, b and c. This periodic orbit is unstable if the slope of the friction force satisfies $\kappa > 2\zeta$. Our system is piecewise-linear, but linearity is not necessary for the general results of this paper. For further reference we use $\mathbf{y} = (x, \dot{x})^T$ and rewrite

3

the system into first-order form

$$\dot{\mathbf{y}} = \begin{cases} A\mathbf{y} + \mathbf{b}_1(t) & \text{if} \quad \dot{x} < v_0, \\ A\mathbf{y} + \mathbf{b}_2(t) & \text{if} \quad \dot{x} > v_0, \end{cases} \tag{2}$$

where

$$A = \begin{pmatrix} 0 & 1 \\ -1 & \kappa - 2\zeta \end{pmatrix},$$

and

$$\mathbf{b}_1(t) = \begin{pmatrix} 0 \\ F_s - \kappa v_0 + u_0 \cos \omega t \end{pmatrix}, \quad \mathbf{b}_2(t) = \mathbf{b}_1(t) - \begin{pmatrix} 0 \\ 2F_s \end{pmatrix}.$$

The switching line in this system is defined by $\dot{x} = v_0$. Our goal is to characterize the dynamics close to the periodic orbit and the switching manifold. To this end we construct a local Poincaré map that takes the discontinuity due to switching into account. In order to construct the local piecewise-linear Poincaré map we make our system autonomous by extending it into three dimensions ($\mathbb{R}^2 \times \mathbb{S}$) with the new coordinates

$$\mathbf{x} = (x_1, x_2, x_3)^T = (x, \dot{x}, t)^T.$$

The switching surface is now defined as

$$\Sigma = \{\mathbf{x} \in \mathbb{R}^2 \times \mathbb{S} : h(\mathbf{x}) = 0\},$$

with $h(\mathbf{x}) = \dot{x} - v_0$ and divides the dynamics into two parts such that

$$\dot{\mathbf{x}} = \begin{cases} \mathbf{f}_1(\mathbf{x}) := \begin{pmatrix} A \begin{pmatrix} x_1 \\ x_2 \end{pmatrix} + \mathbf{b}_1(t) \\ 1 \end{pmatrix} & \text{if} \quad h(\mathbf{x}) < 0, \\ \\ \mathbf{f}_2(\mathbf{x}) := \begin{pmatrix} A \begin{pmatrix} x_1 \\ x_2 \end{pmatrix} + \mathbf{b}_2(t) \\ 1 \end{pmatrix} & \text{if} \quad h(\mathbf{x}) > 0. \end{cases} \tag{3}$$

Equation (3) defines a Filippov system [9] that can exhibit sliding motion along Σ. According to Filippov's definition, the vector field that describes the sliding is obtained as

$$\dot{\mathbf{x}} = \mathbf{f}_{sl} := (1 - \lambda)\mathbf{f}_1(\mathbf{x}) + \lambda \mathbf{f}_2(\mathbf{x}),$$

where $0 \leq \lambda \leq 1$ is such that the dot product $\nabla h(\mathbf{x}) \cdot ((1-\lambda)\mathbf{f}_1(\mathbf{x}) + \lambda \mathbf{f}_2(\mathbf{x})) = 0$. If there is no such λ at a point in Σ, then the corresponding trajectory crosses Σ transversally. For our system (3) we can solve the above equation explicitly and obtain

$$\lambda(\mathbf{x}) = \frac{F_s + u_0 \cos \omega x_3 - x_1 - 2v_0\zeta}{2F_s}.$$

Note that the sliding vector field $\mathbf{f}_{sl} = (v_0, 0, 1)^T$ is constant, which agrees with the physics: when the mass sticks to the belt, it moves with the same constant speed v_0 as
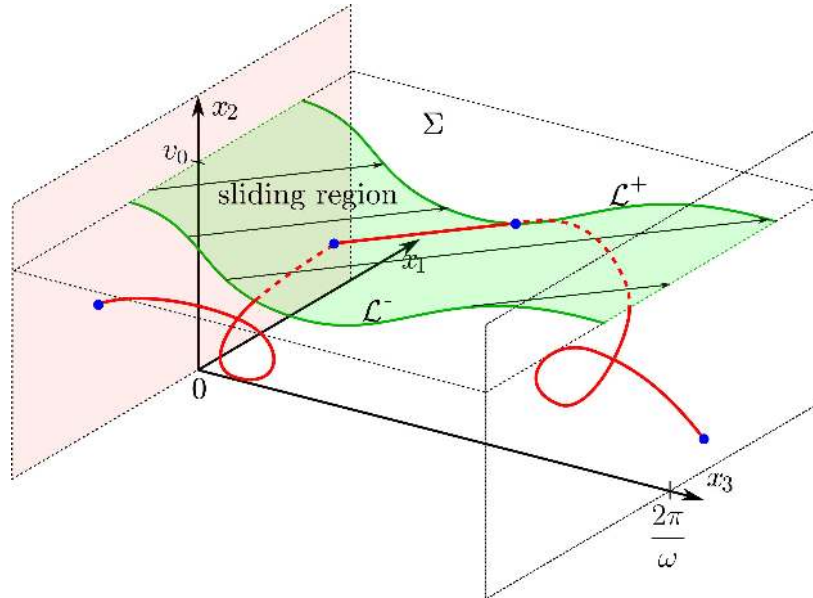
4

Figure 2: Schematic of the phase space of (3). The sliding region is shown in green. A typical trajectory with a sliding segment (red) is shown as an example. When a trajectory hits Σ in between $\mathcal{L}^-$ and $\mathcal{L}^-$ it starts sliding until it reaches $\mathcal{L}^+$.

the belt. The boundary of the sliding region is formed by the two curves $\mathcal{L}^- = \{\mathbf{x} \in \Sigma : \lambda(\mathbf{x}) = 1\}$ and $\mathcal{L}^+ = \{\mathbf{x} \in \Sigma : \lambda(\mathbf{x}) = 0\}$, where either $\mathbf{f}_2$ or $\mathbf{f}_1$ is tangent to Σ. A schematic illustration of the phase space with a typical trajectory is shown in Fig. 2. When the trajectory reaches Σ in the sliding region a non-differentiable change of motion takes place and the trajectory starts to slide until it reaches $\mathcal{L}^+$. Along $\mathcal{L}^+$ $\mathbf{f}_1$ is tangent to Σ, so upon reaching $\mathcal{L}^+$ the trajectory continues following the flow defined by $\mathbf{f}_1$.

Recall that we assume $\kappa > 2\zeta$ so that the trivial periodic orbit Γ is unstable. Because of this instability, system (1) exhibits a stick-slip motion that can lead to complicated dynamics [2, 20]. Here we are interested in the case where Γ is near grazing. The grazing occurs exactly when the forcing amplitude is

$$u_0^* = v_0(\kappa - 2\zeta)\sqrt{1 + \frac{(\omega^2 - 1)^2}{(\kappa - 2\zeta)^2 \omega^2}},$$

and the point on Γ that grazes is

$$\mathbf{x}^* = \left(F_s - \kappa v_0, v_0, \frac{\pi + \tan^{-1} \frac{\omega^2 - 1}{2\zeta - \kappa}}{\omega} \right)^T.$$

If we are not at grazing, $\mathbf{x}^*$ refers to the point on Γ with maximal velocity. We analyze the dynamics in a neighbourhood of $\mathbf{x}^*$ for some $u_0 < u_0^*$ so that the distance between Σ and $\mathbf{x}^*$ is δ and Γ resides in the domain of $\mathbf{f}_1$. Hence, if Γ is close to grazing, all nearby
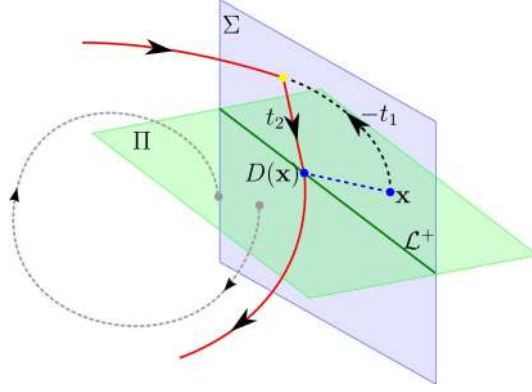
5

Figure 3: The discontinuity map $D(x)$ provides a correction for points on the $\mathbf{f}_2$ side of Σ that accounts for a sliding segment of a trajectory. It follows the flow back from Π to Σ and applies $\mathbf{f}_{sl}$ until $\mathcal{L}^+$ is reached, which by definition is contained in Π.

orbits follow either $\mathbf{f}_1$ or the sliding vector field $\mathbf{f}_{sl}$. We denote the flows corresponding to $\mathbf{f}_1$ and $\mathbf{f}_{sl}$ by $\Phi_1(\mathbf{x}, t)$ and $\Phi_{sl}(\mathbf{x}, t)$, respectively.

We want to investigate the dynamics near the unstable periodic orbit in a Poincaré section. To this end we need to select a Poincaré section Π, that contains the line $\mathcal{L}^+$ and is transversal to both Σ and Γ. The natural choice is

$$\Pi = \{\mathbf{x} \in \mathbb{R}^2 \times \mathbb{S} \; : \; g(\mathbf{x}) := \nabla h(\mathbf{x}) \cdot \mathbf{f}_1(\mathbf{x}) = 0\},$$

which is exactly the surface where h is maximal with respect to the flow $\Phi_1(\mathbf{x}, t)$ generated by $\mathbf{f}_1$. The construction of the associated local Poincaré map is done in two steps. In the first step we disregard the discontinuity and calculate the linear return P map as if Σ does not exist. In the second step we correct the error by constructing the so-called *discontinuity map* D [15]. The actual Poincaré map is then the composition of these two maps, where we first apply D and then P. Hence, let us first focus on this second step and investigate the discontinuity map.

2.1 The discontinuity map

The discontinuity map $D : \Pi \mapsto \Pi$ is a local correction to the smooth Poincaré map P that ignores the switching. The switching surface Σ separates Π into two regions. In one region the flow Φ_1 applies and D is the identity. In the other region applying Φ_1 makes an error that we correct by following a backward trajectory from Π to Σ and applying the sliding vector field $\mathbf{f}_{sl}$ back to Π as should have happened. The schematic of the correction can be seen in Fig. 3. We find $t_1 < 0$ such that $\bar{\mathbf{x}} = \Phi_1(\mathbf{x}, t_1) \in \Sigma$. Then we determine t_2 such that $\Phi_{sl}(\bar{\mathbf{x}}, t_2) \in \Pi$, which defines $D(\mathbf{x})$.

To compute the map from Π to Σ we first approximate the travel time t_1 and then substitute it in the Taylor expansion of the flow $\Phi_1(\mathbf{x}, t_1)$. The time t_1 can be found by solving the equation

$$0 = h(\Phi_1(\mathbf{x}, t_1)), \quad \mathbf{x} \in \Pi. \tag{4}$$

6

The Taylor expansion of this equation at $\mathbf{x}^*$ yields

$$0 = \nabla h \cdot \left(\Delta \mathbf{x} + \frac{t^2}{2} D\mathbf{f}_1 \cdot \mathbf{f}_1(\mathbf{x}^*) \right) + \mathcal{O}(|t|^3 + \|\Delta \mathbf{x}\|^3),$$

from which we obtain time

$$t_1(\mathbf{x}) = \frac{-\sqrt{2\Delta x_2}}{\omega \sqrt{v_0}} + \mathcal{O}(\|\Delta \mathbf{x}\|^{3/2}),$$

and the backward mapping

$$\Phi_1(\mathbf{x}, t_1(\mathbf{x})) = \mathbf{x}^* + \begin{pmatrix} \Delta x_1 - \frac{\sqrt{2\Delta x_2}(v_0+\Delta x_2)}{\omega\sqrt{v_0}} \\ \frac{\sqrt{2\Delta x_2}(\Delta x_1+\Delta x_2(2\zeta-\kappa)+v_0\Delta x_3(\omega^2-1))}{\omega\sqrt{v_0}} \\ \Delta x_3 - \frac{\sqrt{2\Delta x_2}}{\omega\sqrt{v_0}} \end{pmatrix} + \mathcal{O}(\|\Delta \mathbf{x}\|^2),$$

where $\Delta \mathbf{x} = (\Delta x_1, \Delta x_2, \Delta x_3)^T = \mathbf{x} - \mathbf{x}^*$. The sliding part of the trajectory is calculated from the constant sliding vector field $\mathbf{f}_{sl}$ by solving the equation

$$0 = g(\mathbf{x} + t_2 \mathbf{f}_1(\mathbf{x}^*)) = \nabla g(\mathbf{x}^*) \cdot (\Delta \mathbf{x} + t_2 \mathbf{f}_1(\mathbf{x}^*)) + \mathcal{O}(\|\Delta \mathbf{x}\|^2).$$

The calculation of t_2 yields

$$t_2 = \frac{v_0 x_3 + x_2(\kappa - 2\zeta) - \Delta x_1}{v_0 \omega^2} - \Delta x_3 + \mathcal{O}(\|\Delta \mathbf{x}\|^2)$$

and the mapping from Σ to $\mathcal{L}^+ \subset \Pi$ by following $\mathbf{f}_{sl}$ becomes

$$\Phi_{sl}(\mathbf{x}, t_2) = \mathbf{x}^* + \begin{pmatrix} \Delta x_1 - v_0 \Delta x_3 + \frac{v_0 \Delta x_3 + \Delta x_2(\kappa-2\zeta) - \Delta x_1}{\omega^2} \\ v_0 \\ \frac{v_0 \Delta x_3 + \Delta x_2(\kappa-2\zeta) - \Delta x_1}{v_0 \omega^2} \end{pmatrix}.$$

Putting these two flows together we find the discontinuity map

$$D(\mathbf{x}) = \mathbf{x}^* + \begin{pmatrix} \frac{(1-\omega^2)(\sqrt{2}\Delta x_2^{3/2} + \omega(v_0 \Delta x_3 - \Delta x_1)\sqrt{v_0})}{\omega^3 \sqrt{v_0}} \\ 0 \\ \frac{\sqrt{2}}{\omega^3}\left(\frac{\Delta x_2}{v_0}\right)^{3/2} - \frac{\Delta x_1}{\omega^2 v_0} + \frac{\Delta x_3}{\omega^2} \end{pmatrix}.$$

The discontinuity map D contains terms up to order $3/2$ that vanish fast at $\mathbf{x} = \mathbf{x}^*$, so that it is sufficient to take its Jacobian

$$J = \begin{pmatrix} 1 - \frac{1}{\omega^2} & 0 & v_0\left(\frac{1}{\omega^2} - 1\right) \\ 0 & 0 & 0 \\ -\frac{1}{v_0 \omega^2} & 0 & \frac{1}{\omega^2} \end{pmatrix}$$

at $\mathbf{x} = \mathbf{x}^*$ and consider the linear mapping $D(\mathbf{x}) \approx \mathbf{x}^* + J\Delta \mathbf{x}$. Note that J is a projection with a one-dimensional range and a two-dimensional kernel. Therefore, the composition with the smooth Poincaré map P will be piecewise-linear with one part being a projection. In the next section we calculate P and find $P \circ D$.

2.2 The reduced piecewise-linear Poincaré map

The final piecewise-linear Poincaré map is a composition of the discontinuity map D and a smooth return map P that ignores the presence of Σ. This return map P is determined with respect to $\mathbf{f}_1$ around the unstable periodic orbit Γ. We wish to obtain this map in the two-dimensional coordinates $\mathbf{y} = (x, \dot{x})^T$. At a constant time-slice the linear Poincaré map of (2) is represented by the matrix $\mathrm{e}^{A\frac{2\pi}{\omega}}$. To account for additional variation of time on the linear approximation of Π we must use a transformation and obtain the return map $\mathbf{y} \mapsto M\mathbf{y}$, with

$$M = (I - (A + \mathbf{b}_1(x_3^*))\nabla x_3(\mathbf{y}^*))^{-1} \mathrm{e}^{AT} (I - (A + \mathbf{b}_1(x_3^*))\nabla x_3(\mathbf{y}^*)). \tag{5}$$

Here, $x_3(\mathbf{y})$ is the parametrization of the Poincaré section Π as a graph over the plane $x_3 = x_3^* = x_3(\mathbf{y}^*)$ with $\mathbf{y}^* = (x_1^*, x_2^*)^T$. In physical parameters of (1) the matrix M is

$$M = \mathrm{e}^{-\zeta_r T} \begin{pmatrix} \cos \omega_d T + \frac{\zeta(\omega^2+1)}{\omega_d(\omega^2-1)} \sin \omega_d T & \frac{\omega^4 + (4\zeta_r^2-2)\omega^2+1}{\omega_d \omega^2(\omega^2-1)} \sin \omega_d T \\ \frac{\omega^2}{\omega_d - \omega^2 \omega_d} \sin \omega_d T & \cos \omega_d T - \frac{\zeta(\omega^2+1)}{\omega_d(\omega^2-1)} \sin \omega_d T \end{pmatrix}, \tag{6}$$

where $\zeta_r = \frac{2\zeta-\kappa}{2}$, $\omega_d = \sqrt{1 - \zeta_r^2}$ and $T = \frac{2\pi}{\omega}$. The linear approximation of $D(\mathbf{x})$ transformed to the section Π in these coordinates is given by

$$J_2 = \begin{pmatrix} 1 & \frac{2\zeta_r(2\omega^2-1)}{\omega^4} \\ 0 & 0 \end{pmatrix}.$$

We are now ready to construct our local piecewise-linear Poincaré map as the composition

$$F : \mathbf{y} \mapsto \begin{cases} M\mathbf{y} & \text{if } \dot{x} < \delta, \\ MJ_2(\mathbf{y} - \mathbf{y}^*) + M\mathbf{y}^* & \text{if } \dot{x} \geq \delta, \end{cases} \tag{7}$$

where $\mathbf{y}^* = (0, \delta)^T$.

Figure 4 compares direct simulation of (3) with iterations of the piecewise-linear approximation (7). Since (3) is almost linear we expect a close match. Indeed, the main difference between the non-smooth simulation (blue dots) and the iterated map (red dots) is that in (7) we allow points on both sides of Σ, while in the simulation the actual sliding takes place, i.e., orbits cannot cross Σ.

3 Generalized map

In the previous section we constructed a local piecewise-linear Poincaré map from a nonsmooth system with sliding defined by an application. As can be seen in section 2.2, the map F in (7) consists of a linear map with a focus-type unstable fixed point, and a projection. If we consider the system with respect to the eigenvectors of matrix (6) then the focus-type map may be written as

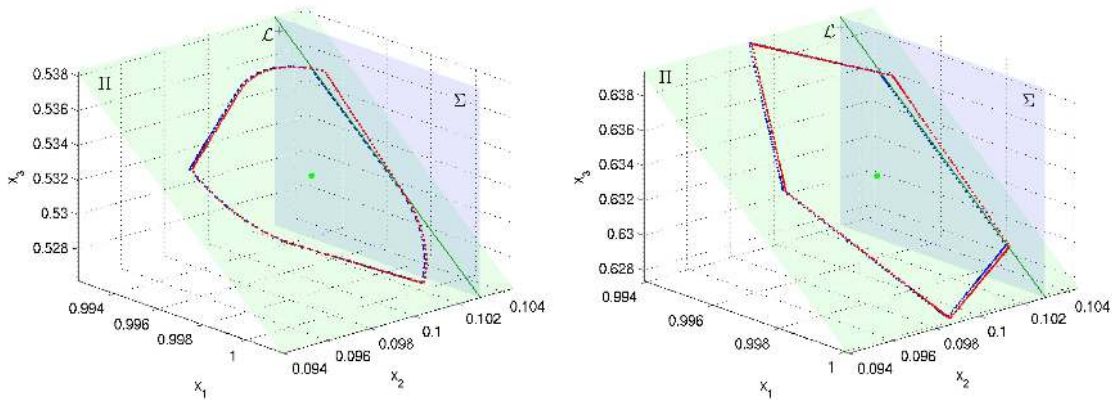$$M = \mathrm{e}^{\beta} \begin{pmatrix} \cos \alpha & \sin \alpha \\ -\sin \alpha & \cos \alpha \end{pmatrix},$$

Figure 4: Simulation result for two different rotation numbers $\alpha = 0.338 \times 2\pi$ and $\alpha = 0.402 \times 2\pi$. The blue dots are direct solution of the Filippov system using Piiroinen's software [19]. The red dots are iterations of the map (7). Other parameters are $F_s = 1$, $\kappa = 0.03$, $\zeta = 0.01$, $u_0 = u_0^*$, $v_0^* = 0.1$ and $v_0 = v_0^* + 0.003$.

where α is the rotation number, and β is the expansion parameter. Similarly, the projection part is of the form

$$J_2 = \begin{pmatrix} 1 & -\cot\gamma \\ 0 & 0 \end{pmatrix},$$

where γ is the angle between the projection direction and the line $\dot{x} = 0$. We assume that $\beta \geq 0$, so that the periodic orbit near grazing-sliding is unstable. Then the generalized map is defined in (7) and can be interpreted as a normal form that describes the phenomena occurring at grazing-sliding with low speeds.

As can be seen in Fig. 4 system (7) has a polygonal-shaped invariant set. Our goal is to examine the properties of the attractor of (7). Since (7) is a normal form, this will give us information about such attractors in all systems with focus-type unstable periodic orbits near grazing sliding. Let us first determine some basic properties of the attractor.

After a certain finite number of iterations every initial point in the phase space will undergo a projection with J_2. Therefore, the only attractor of the system must consist of forward images $\mathcal{K}_n = M^n \mathcal{K}_0$ of $\mathcal{K}_0 = \{\mathbf{y} \in \mathbb{R}^2 : \dot{x} = \delta\}$. Note that the attractor does not include $\mathcal{K}_0$, because after the correction M is applied immediately. After a finite number of iterations of $\mathcal{K}_0$ a polygon is formed around the origin. The invariant set resides on the lines going through the sides of the smallest polygon $\mathcal{P}_f$ around the origin, which we call the *minimal polygon*. Because of the rotation and expansion, $\mathcal{P}_f$ is convex, which means that all vertices fall on the (non-projecting) side of $\mathcal{K}_1$ that contains the origin. This proves that all sides of $\mathcal{P}_f$ are part of the invariant set. Similarly, using $\mathcal{K}_0$ and its preimages, another (smaller) polygon $\mathcal{P}_b$ is formed, which is a downscaled and rotated version of the minimal polygon $\mathcal{P}_f$. These two polygons do

9

not intersect and the lines through the sides of the small polygon will separate regions from which different numbers of iterations are necessary to reach the projecting side of Π. The maximal number of iterations required to reach the projection part of the plane outside $\mathcal{P}_b$ is equal to the number of sides of $\mathcal{P}_b$, which is the same as the number of sides of $\mathcal{P}_f$. Hence, the minimal polygon $\mathcal{P}_f$ is indeed the smallest polygon and its determining lines $\mathcal{K}_i$, $i \in 1, \ldots, q$ contain the attractor.

In order to characterize the attractor further, we count the number sides of $\mathcal{P}_f$ in the next section.

3.1 Number of sides of $\mathcal{P}_f$

The number of sides of the minimal polygon $\mathcal{P}_f$ varies with parameters; the number changes when three different iterates of $\mathcal{K}_0$ intersect at the same point. This point can be determined by stipulating that the intersection of $\mathcal{K}_{n_1}$ and $\mathcal{K}_{n_2}$ lies on $\mathcal{K}_{n_3}$, for some $n_1 < n_2 < n_3$. The intersection point of $\mathcal{K}_{n_1}$ and $\mathcal{K}_{n_2}$ is at

$$\frac{\delta}{\sin(n_1 - n_2)\alpha} \left(\begin{array}{c} e^{n_1\beta} \cos n_2\alpha - e^{n_2\beta} \cos n_1\alpha \\ e^{n_2\beta} \sin n_1\alpha - e^{n_1\beta} \sin n_2\alpha \end{array} \right).$$

Putting this point into the determining equation of $\mathcal{K}_{n_3}$ we obtain the condition

$$e^{n_3\beta} \sin(n_1 - n_2)\alpha + e^{n_2\beta} \sin(n_3 - n_1)\alpha + e^{n_1\beta} \sin(n_2 - n_3)\alpha = 0. \tag{8}$$

Note that equation (8) does not depend on either δ or γ, so that the number of sides of $\mathcal{P}_f$ only changes when varying α or β. Not all triple intersections create a new side on $\mathcal{P}_f$, because they can be formed by higher iterates so that they are outside the minimal polygon $\mathcal{P}_f$. We call triplets (n_1, n_2, n_3) *admissible* if they create a new side on $\mathcal{P}_f$. Note that if a triplet (n_1, n_2, n_3) satisfies (8) then so does $(n_1 + k, n_2 + k, n_3 + k)$, $k \in \mathbb{Z}$. Moreover if (n_1, n_2, n_3) is admissible then $(n_1 + k, n_2 + k, n_3 + k)$ is also admissible as long as the two smallest numbers in the triplet refer to sides of $\mathcal{P}_f$. Because $\mathcal{K}_1$ is always part of $\mathcal{P}_f$ an equivalence class of triplets can be represented by $(1, n_2, n_3)$.

Although the admissible triples are not known (yet), we can numerically construct a chart in the (α, β)-plane that shows all the admissible intersections. Obviously, there is no two-sided polygon so we must iterate $\mathcal{K}_0$ at least three times. In fact, for $\alpha < 2\pi/q$ the minimal polygon will consist of at least $\max(3, q/2)$ sides. Hence, in the first step we construct an initial polygon by iterating $\mathcal{K}_0$ $\max(3, q/2)$ times. At every further iteration we check whether there is an additional intersection with the polygon. If so, we update the polygon, else we record the number of sides. Figure 5 shows the result of the computation.

As we can see in Fig. 5 the number of sides changes along lines that all originate at $\beta = 0$ and connect two neighbouring rotation numbers on the Farey tree. There are three sets of lines. Lines in the first set (red) start at $\beta = 0, \alpha = 2\pi/q$ and tend to $\beta = \infty$; these lines connect $0/1$ and $1/q$ on the Farey tree. Along these lines only one side is added or removed from $\mathcal{P}_f$. Lines of the second type (green) connect two
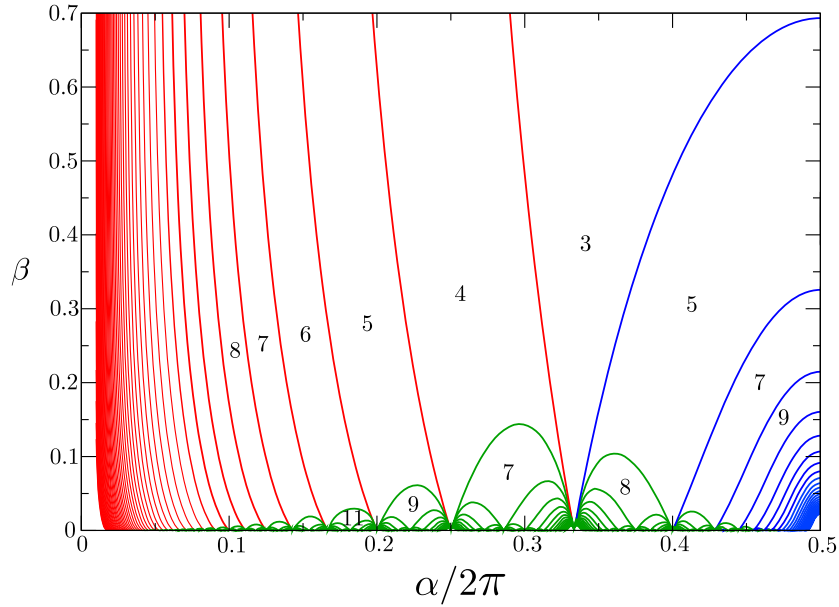
Figure 5: The number of sides of the polygon. The red lines are correspond to polygons with rotation number $1/q$, the green lines are connecting two neighbouring resonant values at $\beta = 0$, and the blue lines connecting the singular rotation number $1/2$ with its Farey neighbours at different levels.

rational rotation numbers of α at $\beta = 0$. The third set of lines (blue) connect $\alpha = \pi$ and its neighbours on the Farey tree at different levels. Note that $\mathcal{P}_f$ is not defined at $\alpha = \pi$. Let us now derive when a triplet of the form $(1, n_2, n_3)$ is admissible.

An empirical approach of constructing admissible triplets

As we noted, all lines in Fig. 5 originate at $\beta = 0$. In the limit $\beta \to 0$ equation (8) becomes

$$4 \sin(n_1 - n_2)\alpha \sin(n_3 - n_1)\alpha \sin(n_2 - n_3)\alpha = 0. \tag{9}$$

Assuming that $\alpha = 2\pi p/q$ it follows that $n_i = n_j + kq$, $i \neq j$ for some $i, j \in \{1, 2, 3\}$. In order to obtain the minimal polygon we choose $k = 1$.

We have also noted that lines in Fig. 5 connect two neighbouring numbers on the Farey tree and that an equivalence class of the admissible triplets can be represented by $(1, n_2, n_3)$. This results in two equations for n_2 and n_3, which yield the four possibilities for the admissible triplets:

$$
\begin{aligned}
(a) &\quad (1, q_1 + 1, q_1 + q_2 + 1), \\
(b) &\quad (1, q_2 + 1, q_1 + q_2 + 1), \\
(c) &\quad (1, q_1 + 1, q_2 + 1), \\
(d) &\quad (1, q_2 - q_1 + 1, q_2 + 1).
\end{aligned}
$$

11

We check these possibilities and find that the last one (d) describes all the lines in the diagram if we allow 0/1 and 1/1 as valid rationals from which the Farey tree is constructed.

The rigorous approach of constructing admissible triplets

In the previous section we based our findings on numerical observations, but we can prove our result rigorously. First we need to prove that every polygon is conjugate to a regular one, that is, the sides follow each other according to a rotation with rotation number p/q. This occurs exactly when sides of the polygon are constructed sequentially with each iteration. Hence, we need to prove the following two steps: a) no complete sides are removed by any iterates of $\mathcal{K}_0$; b) adding vertices stops at some iterate. The proof of a) is trivial, since each iteration places lines farther from the origin. To prove b) we assume a continuously constructed polygon such that $\mathcal{K}_k$ does not add a vertex and the closest vertex to this line is at the intersection of $\mathcal{K}_{n_1}$ and $\mathcal{K}_{n_2}$. Iterating $\mathcal{K}_k$ forward, the closest vertex will be at $(n_1 + j, n_2 + j)$ as long as $n_1 + j \leq q$ and $n_2 + j \leq q$ and the distance uniformly increases, so there is no intersection. However, for further iterates the distance from the vertices increases even more since other vertices of the minimal polygon with smaller iterate numbers will follow, which are closer to the origin. Hence, any further iterate does not intersect $\mathcal{P}_f$ anymore.

Let us now assume that the order of the sides of $\mathcal{P}_f$ corresponds to the rotation number p/q. We write this rotation number as the Farey addition

$$\frac{p}{q} = \frac{p_1 + p_2}{q_1 + q_2}$$

of two neighbouring rational numbers p_1/q_1 and p_2/q_2. We are looking for transitions when three neighbouring sides of $\mathcal{P}_f$ start to intersect at one point and the side in the middle is removed. Without loss of generality we can assume that this happens at the first iterate $\mathcal{K}_1$. Obviously, $\mathcal{K}_1$ cannot be excluded from the polygon, therefore, either its left or its right neighbour will vanish. If the rotation number is decreasing from p/q then the left neighbour will vanish, and if it is increasing the right neighbour will vanish. We assume that the right and left neighbours are the n_Rth and the n_Lth iterate of $\mathcal{K}_1$, respectively; see also Fig. 6. Because of the p/q rotation these numbers can be calculated as

$$n_R \frac{p}{q} = k_R + \frac{1}{q} \quad \text{and} \quad n_L \frac{p}{q} = k_L - \frac{1}{q},$$

where n_R, n_L, k_R and k_L are integers. After a simple rearrangement it turns out that these equations are the Farey conditions for neighbouring Farey numbers, i.e.,

$$\frac{p}{q} - \frac{k_R}{n_R} = \frac{1}{q n_R} \quad \text{and} \quad \frac{k_L}{n_L} - \frac{p}{q} = \frac{1}{q n_L}.$$

Because we constructed p/q from two consecutive numbers on the Farey tree, it follows that $n_R = q_1$, $n_L = q_2$, $k_R = p_1$ and $k_L = p_2$. Note that here the L and R indices
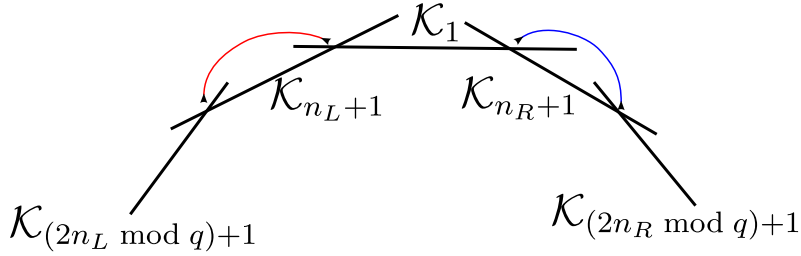
12

Figure 6: A triple intersection at $\mathcal{K}_1$ must cause removal of either neighbouring side $\mathcal{K}_{n_L+1}$ or $\mathcal{K}_{n_R+1}$, depending on whether the rotation number is decreasing or increasing from p/q, respectively.

might need to be interchanged. Regularity implies that the subsequent neighbours are iterates $2n_R \bmod q$ and $2n_L \bmod q$ of $\mathcal{K}_1$ to the right and left, respectively. Assuming that $q_1 < q_2$ we get the possible triplets

$$(1, 2n_R \bmod q, n_R + 1) = (1, 2q_1 + 1, q_1 + 1) \tag{10}$$

and

$$(1, 2n_L \bmod q, n_L + 1) = (1, q_2 - q_1 + 1, q_2 + 1). \tag{11}$$

Substituting (10) into (8) gives $\sin q_1 \alpha = 0$, which is a spurious result. However, (11) yields a valid triplet, that represents the set of lines that start from $\beta = 0$ and connect the rotations numbers p_1/q_1 and p_2/q_2. With this analysis we can now construct Fig. 5 by implicitly plotting the solutions of (8) for different admissible triplets.

3.2 One-dimensional dynamics on the attractor

The dynamics on the polygonal-shaped attractor can be reduced to the switching line $\mathcal{K}_0$ by taking into account how many iterations are necessary to reach the projection region again. Therefore, we subdivide the phase plane into regions S_m from which m iterations bring a point to the other side of $\mathcal{K}_0$. These regions are separated by preimages of $\mathcal{K}_0$ in such a way that the first preimage $\mathcal{K}_{-1}$ divides the phase plane into two half planes one of which maps to the other side of $\mathcal{K}_0$ after one iterate. The other half plane is divided by the second preimage $\mathcal{K}_{-2}$ into two regions of which one maps to the other side of $\mathcal{K}_0$ after two iterates, and so on. Assuming a p/q rotation number of the minimal polygon, we need to consider up to q preimages to cover fully the switching line with regions S_i, $1 \leq i \leq q$. Recall that the number of regions covering $\mathcal{K}_0$ depends on α and β, but not on γ. The resulting equation is of the form

$$\mathbf{y} \mapsto \mathbf{y}^* + J_2(M^m \mathbf{y} - \mathbf{y}^*), \quad \mathbf{y} \in S_m \cap \mathcal{K}_0, \tag{12}$$

with $\mathbf{y} = (x, \delta)$. We note that this equation does not guarantee that the dynamics will stay in between the vertices of the polygon, so that it is not possible to describe the dynamics along the arclength of the polygon.
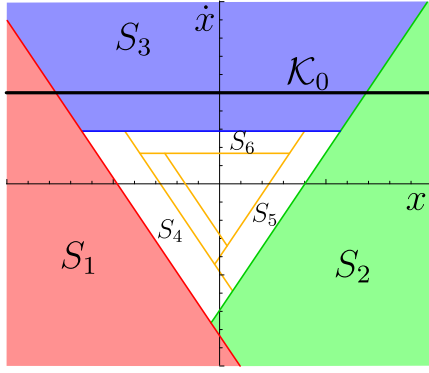
Figure 7: Subdivision of the phase space into regions S_k from which k iterations with M are necessary to map points over the switching line. The picture holds qualitatively for all $\alpha = 2\pi/3$, $\beta > 0$.

In what follows we present the special case, where the minimal polygon has three sides at $\alpha = 2\pi/3$ and $\beta = \log 1.2$. The subdivision of the phase space can be seen in Fig. 7. There are three regions S_1, S_2 and S_3 that cover $\mathcal{K}_0$, therefore the one-dimensional map will consist of three pieces. Initial points from other regions S_k, $k > 3$ will reach the attractor in finitely many steps. Figure 8 shows the one-dimensional map for $\alpha = 2\pi/3$, $\beta = \log 1.2$ and four different projection angles γ. For $\gamma = 0.75\pi$ a period-two attractor exists; see Fig. 8.(a). This attractor is stable because the product of the absolute slopes of the map on the left and the right side is smaller than unity. Note that a point in the middle interval must be interpreted as three iterations and a point on the right half line indicates two iterations on the attractor. Therefore, the period-two attractor has period three on the polygonal-shaped invariant set. Increasing γ leads to period doubling after which immediate chaos arises; see Fig. 8.(b)-(c). Using simulation it can be demonstrated that the attractor in Fig. 8.(c) is indeed chaotic. In the inset of Fig. 8.(c) there are two intervals, denoted by 0 and 1, that are mapped onto each other. Using the overlap of the intervals and their images a so-called transition matrix can be constructed such that its (i, j)th element is one or zero depending on whether the image of interval j contains the interval i or not. The matrix for our example is

$$\begin{pmatrix} 1 & 1 \\ 1 & 0 \end{pmatrix}.$$

This matrix is irreducible, because its second power has only non-zero elements. According to the theory of symbolic dynamics this means that the motion is chaotic [13, 25].

Increasing γ even further the attractor shrinks to a point at a certain parameter value and after a crisis the attractor extends to a rather large interval. Because the absolute slope of the map is greater than one everywhere, there cannot be any stable periodic orbit, which again means that the attractor must be chaotic. In system (12) quasi-periodicity is unlikely.
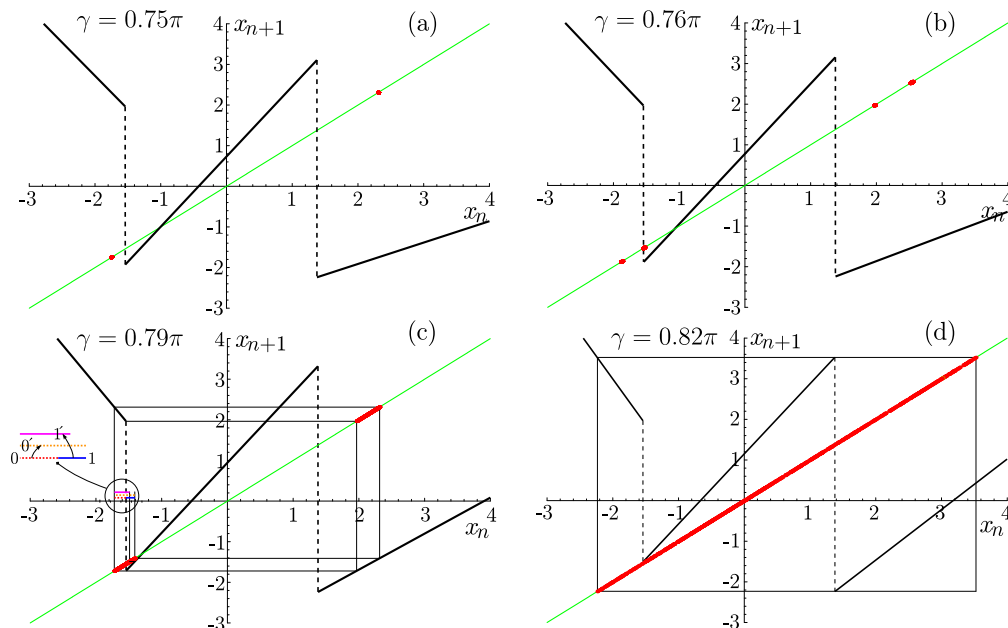
14

Figure 8: Return maps on the switching line $\mathcal{K}_0$ as a function of the projection angle γ. A period two attractor (a) undergoes a period doubling bifurcation (b), which induces a chaotic motion (c). The chaotic attractor shrinks to a point and a new, lager attractor arises (d).

Figure 9 shows the shape of the attractor (red) for all the four cases that are shown in Fig. 8. It is apparent that not the minimal polygon $\mathcal{P}_f$ but the (black) lines defining $\mathcal{P}_f$ contain the attractor. The chaotic motion is a consequence of stretching and non-invertibility of the dynamics on the attractor.

For polygons with higher number of sides it is not straightforward to give a characterisation of the dynamics. Indeed, fairly complete theory is only developed for discontinuous maps on two intervals (see e.g. [10]), and only an abstract characterization is available for more general systems [11].

4   Conclusions

In the previous sections we have seen that a polygonal-shaped attractor can arise when a focus-type unstable periodic orbit is near to a generic grazing-sliding bifurcation. We deduced a three-parameter piecewise-linear map that completely describes this phenomenon in the plane. We counted the number of sides of this polygon and characterized how it depends on the parameters. Finally, we showed that the dynamics can be described by a discontinuous interval map which can exhibit periodic and chaotic motions.

We think of the polygonal-shaped attractor as the analog of an invariant torus in a smooth vector field. At the moment when the unstable periodic orbit inside it grazes
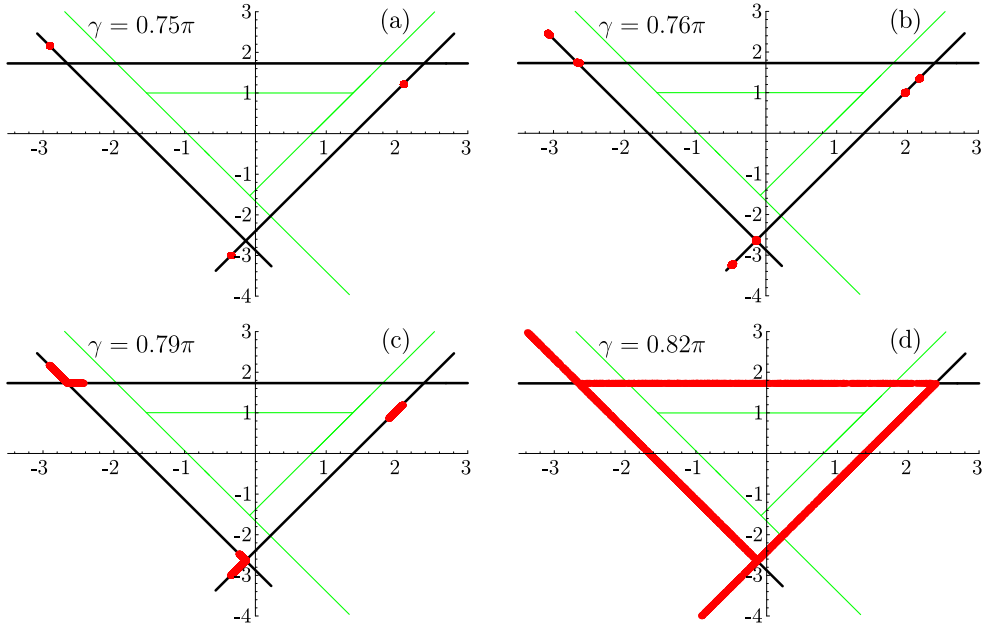
15

Figure 9: The shape of the attractor at the same parameter values as in Fig. 8. Note that the minimal polygon $\mathcal{P}_f$ does not contain the attractor indicated by red dots.

the sliding region, the polygonal-shaped attractor disappears and the periodic orbit becomes stable. Hence, we could relate this bifurcation to a supercritical Neimark-Sacker bifurcation. An invariant torus in a smooth vector field typically persists only for relatively small smooth perturbations, but the polygonal-shaped attractor appears to be far more robust than a smooth invariant torus. Similar analogs for invariant tori have been studied in different contexts; for example in Filippov systems without sliding [26] and systems with impact [4, 23].

We believe that our analysis can also be applied in the context, where an attractive smooth invariant torus undergoes a grazing-sliding bifurcation. Clearly, before grazing we have an attracting torus in a smooth three-dimensional vector field. Hence, this stable torus has an unstable object inside it, which is either a periodic orbit or another torus. In general we would expect that the torus breaks up either before or at the moment of grazing. However, if we assume that the torus persists up to the grazing point, the inside unstable object will determine the dynamics. Regardless of whether the object inside is an unstable periodic orbit or a repelling torus, our construction of polygons will remain valid with the exception that the rotation and expansion now will be completely nonlinear. Hence, a polygonal-shaped attractor appears and in this sense the torus persists past the grazing-sliding bifurcation. On the other hand, most probably the dynamics on the attractor is chaotic, so that in this sense the torus breaks up at grazing-sliding.

Non-smooth bifurcations most of the time do not persist if the dimension of the system changes. It remains to be analyzed whether this is the case of the polygonal-

16

shaped attractors. Therefore, our future work will include the study of systems where a three dimensional attracting slow manifold contains the grazing-sliding dynamics.

References

[1] P. Casini, O. Giannini, and F. Vestroni. Experimental evidence of non-standard bifurcations in non-smooth oscillator dynamics. *Nonlinear Dyn.*, 46:259–272, 2006.

[2] G. Csernák and G. Stépán. On the periodic response of a harmonically excited dry friction oscillator. *J. Sound Vibrat.*, 295:649–658, 2006.

[3] F. B. Cunha, D. J. Pagano, and Moreno U. F. Sliding bifurcations of equilibria in planar variable structure systems. *IEEE Trans. Circ. & Syst. I*, 50(8):1129–1134, 2003.

[4] H. Dankowicz, P. Piiroinen, and A. B. Nordmark. Low-velocity impacts of quasiperiodic oscillations. *Chaos Solitons & Fractals*, 14(2):241–255, 2002.

[5] M. di Bernardo, C. J. Budd, A. R. Champneys, and P. Kowalczyk. *Bifurcation and chaos in piecewise-smooth dynamical systems: Theory and applications.* Springer, to be published.

[6] M. di Bernardo, P. Kowalczyk, and A. Nordmark. Sliding bifurcations: a novel mechanism for sudden onset of chaos in dry friction oscillators. *Internat. J. Bifur. Chaos Appl. Sci. Engrg.*, 13(10):2935–2948, 2003.

[7] R. D. Eyres, P. T. Piiroinen, A. R. Champneys, and N. A. J. Lieven. Grazing bifurcations and chaos in the dynamics of a hydraulic damper with relief valves. *SIAM J. Applied Dynamical Systems*, 4(4):1076–1106, 2005.

[8] B. Feeny and F. C. Moon. Chaos in a forced dry friction oscillator: experiments and numerical modelling. *J. Sound Vibrat.*, 170(3):303–323, 1994.

[9] A. F. Filippov. *Differential Equations with Discontinuous Right-Hand Sides.* Kluwer Academic, Dordrecht, 1988.

[10] S. J. Hogan, L. Higham, and T. C. L. Griffin. Dynamics of a piecewise linear map with a gap. *Proc. R. Soc. A*, 463:49–65, 2007.

[11] A. J. Homburg. Piecewise smooth interval maps with non-vanishing derivative. *Ergod. Th. & Dynam. Sys.*, 20:749–773, 2000.

[12] A. C. J. Luo and B. C. Gegg. Stick and non-stick periodic motions in periodically forced oscillators with dry friction. *J. Sound Vibrat.*, 291:132–168, 2006.

[13] J. Moser. *Stable and Random Motions in Dynamical Systems*. Princeton University Press, Princeton, 1973.

[14] S. Narayanan and K. Jayaraman. Chaotic vibration in a non-linear oscillator with coulomb damping. *J. Sound Vibrat.*, 146(1):17–31, 1991.

[15] A. B. Nordmark. Non-periodic motion caused by grazing incidence in an impact oscillator. *J. Sound Vibrat.*, 145(2):279–297, 1991.

[16] B. Novák, Zs. Pataki, A. Ciliberto, and J. J. Tyson. Mathematical model of the cell division cycle of fission yeast. *Chaos*, 11(1):277–286, 2001.

[17] J. Nussbaum and A. Ruina. A two degree-of-freedom earthquake model with static/dynamic friction. *Pure and Applied Geophysics*, 125(4):629–656, 1987.

[18] M. Oestreich, N. Hinrichs, and K. Popp. Bifurcation and stability analysis for a non-smooth friction oscillator. *Archive of Applied Mechanics*, 66(5):301–314, 1996.

[19] P. T. Piiroinen and Y. A. Kuznetsov. An event-driven method to simulate filippov systems with accurate computing of sliding motions. *ACM Transactions on Mathematical Software*, 34(3), 2008.

[20] K. Popp and P. Stelter. Stick-slip vibration and chaos. *Phil. Trans. R. Soc. Lond. A*, 332:89–105, 1990.

[21] J. Sieber, P. Kowalczyk, S.J. Hogan, and M. di Bernardo. Dynamics of symmetric hybrid dynamical systems with delay. *Preprint*, pages 1–29, 2007. http://www.abdn.ac.uk/˜eng824/documents/SKHD07.pdf.

[22] I. Sushko, T. Puu, and L. Gradini. The hicksian floor-roof model for two regions linked by interregional trade. *Chaos, Solitons & Fractals*, 18:593–612, 2003.

[23] P. Thota and H. Dankowicz. Continuous and discontinuous grazing bifurcations in impacting oscillators. *Physica D*, 214(2):187–197, 2005.

[24] V. I. Utkin. *Sliding modes in control and optimization*. Springer, 1992.

[25] S. Wiggins. *Global bifurcations and chaos*. Springer, 1988.

[26] Z. T. Zhusubaliyev, E. Mosekilde, S. Maity, S. Mohanan, and S. Banerjee. Border collision route to quasiperiodicity: Numerical investigation and experimental confirmation. *Chaos*, 16(2):023122/11, 2006.